Formation flying orbits and GNC design in binary asteroid systems

Andrea Capannolo[a], Giovanni Zanotti[a,*], Michèle Lavagna[a], Giuseppe Cataldo[b]

[a]Politecnico di Milano - Aerospace Science and Technology Department, Via G. La Masa, 34, Milano 20156, Italy
[b]NASA Goddard Space Flight Center, 8800 Greenbelt Rd, Greenbelt, MD 20771, United States

Received 1 May 2013; Received in final form 10 May 2013; Accepted 13 May 2013;
Available online 15 May 2013

Abstract

Formation flying represents a promising opportunity for next space missions, due to its benefits in cost saving, redundancy and fault tolerance given by multiple small and cheap space segments exploitation, with comparable performance of a single, large monolithic spacecraft. That is even more relevant in asteroid exploration, as the harsh environment poses great risks to the probes survival. The low, irregular gravity field, the poor knowledge of shape and composition, and the possible presence of floating particles in the surroundings suggest adopting a low-risk strategy for the exploration of these bodies, delegating proximity operations to multiple nanosatellites, while keeping the main spacecraft at safe distance. As a downside, multiple cooperating spacecraft imply advanced capabilities in accurately reconstructing the relative positions and displacements and in fixing reconfiguration manoeuvres. Moreover, whenever relative distance is very close, agents' guidance and control shall be autonomously computed by the spacecraft, as promptness of commands is not ensured relying on ground segment only. The partially unknown environment exacerbates this issue, demanding navigation and control schemes capable of withstanding potentially large uncertainties in the dynamics. If a binary system is considered, the multiple gravitational sources complicate even more the setup of the formation, requiring an accurate search and selection of operative orbits. This study will be thus defined by three different steps. First the search and development of suitable trajectories to host a reconfigurable satellite formation is carried out. Then the design of a Model Predictive on-board guidance and control law is performed to assess the capability of the spacecraft to execute successful reconfiguration transfers relying on a simplified dynamical model (namely the Circular Restricted Three-Body Problem). At the end the navigation error requirements are derived, in order to ensure the feasibility of the guidance and control scheme. Inspired by the Hera mission, this study explores the aforementioned aspects of the design of a formation for the exploration of the Didymos binary asteroid system, which comprises many complications but also challenges for many other future missions to fly in unexplored environments.

Keywords: Formation Flying ; Model Predictive Control ; Navigation ; Asteroid Exploration ; Autonomous GNC

1. Introduction

The foreseeable future of space exploration will strongly rely on new systems with a considerable level of on-board autonomy. The benefits from the development of autonomous systems are twofold. The first one is represented by the several mission scenarios unlocked by exploiting on-board systems that rely on ground segment little or not at all. The second benefit is the reduction of mission operations costs, which may represent a limiting factor for some classes of space missions, such as low-budget ones.

*Corresponding author: giovanni.zanotti@polimi.it

Among the spacecraft design aspects, the *Guidance Navigation and Control* (GNC) scheme represents one of the most critical fields for the success of the mission. Because of that, the introduction of autonomy in the GNC loop must ensure a certain degree of robustness to errors between on-board dynamical models and the actual dynamics of the spacecraft.

Many advanced mission concepts are based on the exploitation of multiple, cooperating spacecraft. This concepts require the definition of specific relative GNC constraints, particularly in terms of safety. In such scenarios, it is paramount to avoid failures in the relative state estimation and control, which may lead to collisions among the agents of the formation.

Among the scenarios that may largely benefit from an autonomous systems, the exploration of small bodies of the Solar System stands out. The great limitations given by the uncertainties of the environment (shape and size of the attractor, irregular gravity field, etc.), and the lack of promptness in the ground control due to the large distance from Earth, would enormously benefit from an autonomous GNC scheme, where the spacecraft could react in real time to local changes in the expected behaviour of the dynamics.

An interesting test scenario for autonomous GNC algorithms is certainly represented by the Didymos binary asteroid system, target of the first human attempt to test a hypervelocity kinetic impact for small body trajectory deflection. Within the AIDA (*Asteroid Impact and Deflection Assessment*) framework Cheng et al. (2015), the American spacecraft DART (*Double Asteroid Redirection Test*) Ozimek and Atchison (2017) crashed the moonlet of the system, Dimorphos, on purpose, while the CubeSat named LICIACube (*Light Italian CubeSat for Imaging of Asteroids*) Dotto et al. (2021); Capannolo et al. (2021) performed a fly-by to image the impact and map the evolution of ejected material. About 4 years after the impact, the European Hera mission Michel et al. (2020) will reach the binary to perform accurate measurements of the impacted body, exploiting two CubeSats for close scientific observations and measurements.

Within this scenario, this paper leverages recent developments of the trajectory and GNC design topics Capannolo et al. (2020); Piccinin et al. (2020); Silvestrini et al. (2021), extending them in the field of small bodies exploration. In particular, an adaptive guidance and control scheme for formation maintenance and reconfiguration, previously developed for cislunar applications Capannolo et al. (2023), is here tuned and tested for a formation of two CubeSats within the Didymos binary asteroid system environment, extending the analysis with considerations on state estimation errors and applicability in a closed loop GNC scheme. After this introduction, Section 2 will go through the dynamical framework presentation, and the selection and development of the operative orbits that will be used to host the formation. Then, Section 3 will present the design of the controller for the formation. An adaptive *Model Predictive Guidance and Control* scheme (MPC) is developed, and results obtained under different constraints and conditions are shown, together with the validation results obtained in a high-fidelity dynamical representation. Section 4 will go through some preliminary navigation considerations, deriving the estimation accuracy requirements to be satisfied within the GNC loop by a navigation filter. Finally, some concluding remarks and possible improvements of the overall strategy are discussed in Section 5.

2. Dynamics of the formation

2.1. Gravitational models

The following paragraphs briefly describe the various gravitational models exploited for the analyses.

Point mass gravity. The simplest way of representing the gravitational field of a massive object is through the *point mass model*, where all the mass is shrunk in its center of mass, and reads

$$U = \frac{Gm}{r} \tag{1}$$

where G is the gravitational constant, m represents the overall attractor's mass, and r is the distance of the spacecraft from the attracting point mass. Despite the gravity fields of asteroids are typically far from being perfectly spherical, this model is still useful for the preliminary design of the formation.

Spherical Harmonics gravity. The *spherical harmonics expansion model* is a computationally convenient approach when the irregularities of the attractor's shape need to be modelled. Its expression, following Hobson (1931), reads

$$U_{\text{she}} = \frac{Gm}{r}\left\{1 + \sum_{i=2}^{n}\sum_{j=0}^{i}\left(\frac{R_0}{r}\right)^i\Big[C_{ij}\cos(j\lambda) + S_{ij}\sin(j\lambda)\Big]P_{ij}(\cos(\theta))\right\} \tag{2}$$

where λ and θ are the attractor's longitude and co-latitude respectively, R_0 a reference radius (typically the average equatorial radius), $P_{ij}(x)$ are *Associated Legendre Polynomials*, as described in Belousov (2014), while C_{ij} and S_{ij} are the normalised Stokes coefficients, computed as

$$\begin{aligned} C_{ij} &= \frac{1}{m}\sqrt{\frac{(2-\delta_{0j})(i-j)!}{(2i+1)(i+j)!}}\iiint_m \left(\frac{r}{R_0}\right)^i P_{ij}(\sin(\theta))\cos(j\lambda)dm \\ S_{ij} &= \frac{1}{m}\sqrt{\frac{2(i-j)!}{(2i+1)(i+j)!}}\iiint_m \left(\frac{r}{R_0}\right)^i P_{ij}(\sin(\theta))\sin(j\lambda)dm \end{aligned} \tag{3}$$

with

$$\delta_{0j} = \begin{cases} 1 & (j=0) \\ 0 & (j\neq 0) \end{cases} \tag{4}$$

Ellipsoid gravity. The *ellipsoidal model* is an analytical expression derived by MacMillan (1958), particularly useful when short distances are present between spacecraft and attractor, as long as the latter is well approximated by a triaxial ellipsoid shape. The formulation has the advantage over the spherical harmonics model of being valid also within the Brillouin sphere, down to the surface of the object. According to MacMillan, the potential of a field point reads

$$\begin{aligned} U_{\text{ell}} = &\frac{2G\rho\pi abc}{\sqrt{a^2-c^2}}\Bigg\{\left[1 - \frac{x^2}{a^2-b^2} + \frac{y^2}{a^2-b^2}\right]F(\omega_\kappa, k) + \left[\frac{x^2}{a^2-b^2} - \frac{(a^2-c^2)y^2}{(a^2-b^2)(b^2-c^2)} + \frac{z^2}{b^2-c^2}\right]E(\omega_\kappa, k) + \\ &+ \left[\frac{(c^2+\kappa)y^2}{b^2-c^2} - \frac{(b^2+\kappa)z^2}{b^2-c^2}\right]\frac{\sqrt{a^2-c^2}}{\sqrt{(a^2+\kappa)(b^2+\kappa)(c^2+\kappa)}}\Bigg\} \end{aligned} \tag{5}$$

with a, b, c being the three semi axes in descending length order, x, y, z the field point coordinates in the reference frame aligned with the semi axes, ρ the average density of the attracting body, F and E the Legendre's elliptic integrals of first and second kind, and ω_κ and k satisfy the following conditions:

$$\sin(\omega_\kappa) = \sqrt{\frac{a^2-c^2}{a^2+\kappa}} \tag{6}$$

$$k^2 = \frac{a^2-b^2}{a^2-c^2} \tag{7}$$

The previous equations show an additional parameter (κ), which is defined as the largest algebraic root of the following equation:

$$\frac{x^2}{a^2+\kappa} + \frac{y^2}{b^2+\kappa} + \frac{z^2}{c^2+\kappa} = 1 \tag{8}$$

2.2. Dynamical model

CRTBP. The Circular Restricted Three-Body Problem (CRTBP) describes the motion of a point mass m_3, subjected to the gravitational attraction of two primary objects, m_1 and m_2, assumed to orbit on a circular path around their center of mass (CoM) Szebehely (1967). By expressing the dynamics in a rotating frame, where the two attractors appear fixed, the equations of motion read

$$\begin{aligned} \ddot{x} - 2\dot{y} &= \frac{\partial \mathcal{U}}{\partial x} \\ \ddot{y} + 2\dot{x} &= \frac{\partial \mathcal{U}}{\partial y} \\ \ddot{z} &= \frac{\partial \mathcal{U}}{\partial z} \end{aligned} \tag{9}$$

Here, an adimensionalisation has been introduced, by scaling the quantities with respect to the total mass of the binary system, to the distance from the attractors, and to the gravitational constant. The quantity $\mathcal{U}$ is the pseudo-potential function, and reads

$$\mathcal{U} = \frac{1}{2}(x^2 + y^2) + \tilde{U}_1 + \tilde{U}_2 \tag{10}$$

where $\tilde{U}_1$ and $\tilde{U}_2$ are the separate gravitational potentials of the two attractors (whose expressions vary according to the selected model as per Equations (1),(2),(5)), properly made nondimensional according to the previously mentioned scaling.

Ephemeris model. When a high-fidelity modelling of the dynamics is required, it is fundamental to rely on accurate history of the positions of all attractors and generators of perturbation. This can be done, through the *ephemerides*, tables of state and time data of celestial object created through highly accurate models and several observation of the bodies' motion Folkner et al. (2014). The disadvantage of this model is the lack of regularity and periodicity, which makes the search of orbital solutions a very difficult task. Indeed, this level of fidelity can be applied to already found solutions in the CRTBP (or other simplified dynamical models) to refine the trajectories and their performance.

2.3. Target asteroid system: 65803 Didymos

The "65803 Didymos" binary system (depicted in Fig. 1) consists of a main asteroid (Didymos) with an irregular shape and a maximum diameter of 820 m, and a moonlet (Dimorphos) with an expected ellipsoidal shape, and a maximum diameter of 206 m. The main asteroid has a spin period of 2.26 h. The moonlet orbits around the primary on a nearly circular orbit, at an average distance of 1180 m and a period of 11.92 h. The system's parameters are derived from on-ground observations Pravec et al. (2006); Scheirich and Pravec (2009): mean values and range of uncertainty of the most relevant ones are reported in Table 1, where a_m, e_m and T_m are the moonlet's orbit semi-major axis, eccentricity and period respectively, M_{tot} is the total mass of the binary system, $\frac{m_2}{m_1}$ is the mass ratio between the moonlet and the primary asteroid, and ρ is the average density of both bodies.

2.4. Operative orbit

To properly initialise a formation, it is fundamental to search for a reference orbit that is sufficiently stable and suitable for the objectives of the mission. Previous works have demonstrated how some orbits in the CRTBP model of the Didymos system are strongly affected by the irregularity of the attractors' shape (see Capannolo et al. (2019)). Furthermore, the low intensity of the gravity makes the effect of the *Solar Radiation Pressure* (SRP) particularly critical for the stable or unstable behavior of the trajectory. Among the typical orbital families studied in the framework of the CRTBP (see Chappaz (2015)), it has been shown how the *Distant Retrograde Orbits* (DRO) are very stable, and remain bounded even in presence of large perturbations from the SRP

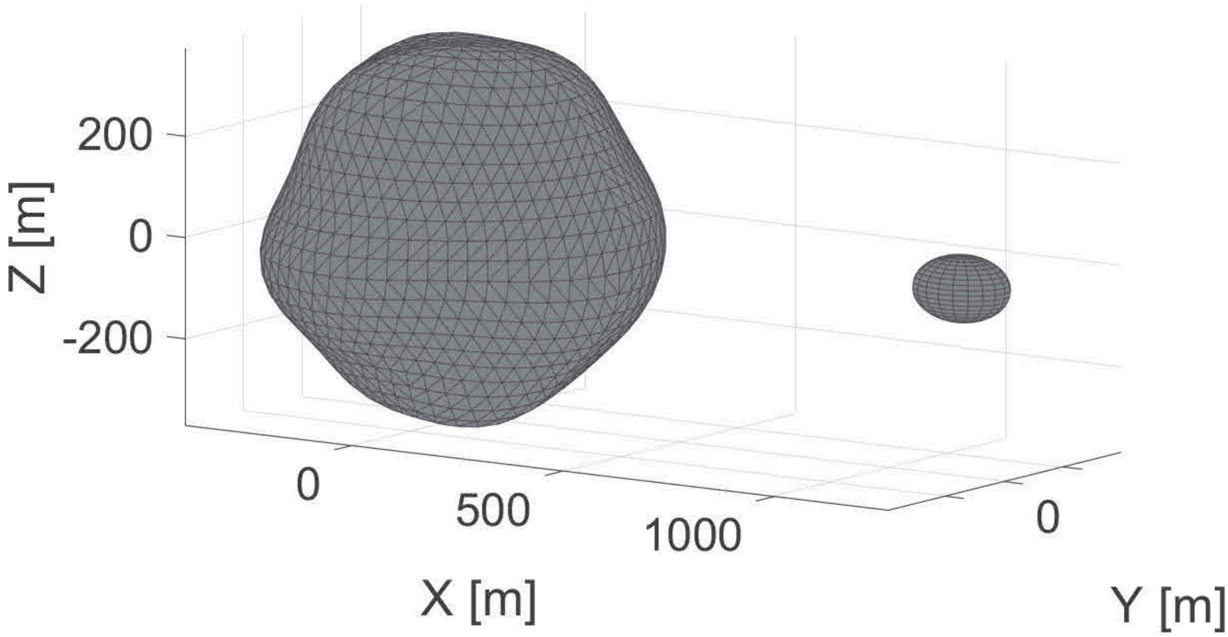

Fig. 1: 65803 Didymos

and Sun's gravity (fourth body), as depicted in Fig. 2. In particular, medium-sized DROs display the best stability, thanks also to their larger distance from both the attractors, and are therefore selected as final operative orbits. In particular, the selected DRO is the one depicted in Fig. 2, having a period of 10.73 h, with a resonance of 9/10 with Didymoon period.

2.5. *Formation setup: Quasi-Periodic Invariant Tori*

Once the operative orbit is selected, a naturally bounded formation can be built by leveraging the dynamical properties of the periodic orbits in the CRTBP. In particular, periodic orbits possess a neighbouring region of quasi-periodic motion which preserves the same orbital frequency (ω_0), plus a secondary frequency (ω_1) of *winding* motion around the periodic reference. The two frequencies are incommensurable, i.e. the trajectory never closes itself (hence the term *quasi-periodic*), and a propagation to infinity of this motion will generate a surface (the *torus*) rather than a curve, parametrised by two angles corresponding to the two aforementioned frequencies, *longitude* and *phase* respectively (θ_0 and θ_1). Then, a bounded leader-follower formation can be built by placing one spacecraft on the reference periodic orbit, and the others on the quasi-periodic torus Barden (1998).

The procedure to generate quasi-periodic tori follows the same scheme used for generating families of periodic orbits, and consists of an initialisation using the center manifold of the periodic orbit, a correction in the nonlinear regime, and a continuation along some specified parameter, as in Baresi et al. (2018). The full set of equations and conditions used in this paper can be found in Capannolo (2022); Capannolo and Lavagna (2020). The result of the process is a family of quasi-periodic tori, with variable size (distance from the reference periodic orbit) and secondary (or winding) frequency. Note than the main frequency is not varied in

Parameter	Value
a_m	1180^{+157}_{-79} [m]
e_m	$0.02^{+0.01}_{-0.02}$ [-]
T_m	$11.920^{+0.005}_{-0.005}$ [h]
M_{tot}	$5\,278^{+0.54}_{-0.54}\times 10^{11}$ [kg]
$\frac{m_2}{m_1}$	$0.0093^{+0.0039}_{-0.0039}$ [-]
ρ	$2104^{+631.2}_{-631.2}$ [kg m^{-3}]

Table 1: 65803 Didymos estimated parameters

the continuation process, otherwise the agents of the formation on the torus would have a secular drift from the leader spacecraft on the periodic orbit.

The DRO family possesses two couples of complex conjugates eigenvalues, meaning that two potential tori families can be developed. One couple identifies the quasi-periodic planar motion ($x - y$ plane of the synodic frame), while the second couple describes an out-of-plane oscillatory motion. With the idea of leveraging the formation for a characterisation of the binary system (e.g. stereoscopic observation of the bodies' surface), it is desirable to keep the distance of each agent from the asteroid surface as equal as possible, and to avoid mutual passages in front of their respective fields of view. For this reason, the out-of-plane motion is here considered for the development of the formation.

The single torus within the family is identified by the distance d of the longitude/phase $(0°, 0°)$ point from the main spacecraft on the reference periodic orbit. The 0° longitude point is here considered as the point of the DRO aligned with the two asteroids, and between them. The family is developed from a minimum d value of 10 m, up to the maximum value that ensured the existence of a quasi-periodic solution, equal to 73.62 m. Figures 3 and 4 depict the smallest and largest developed tori in the binary system's frame, and relatively to a spacecraft orbiting on the reference periodic DRO.

Notice that the initially (linearised) pure vertical motion, acquires an $x - y$ oscillatory mode when continuing the family in the nonlinear regime. Among the possible operative trajectories, the largest one represents the most challenging for formation control, because of its larger nonlinearities. For this reason, it has been selected as study case. The main characteristics of the trajectory are reported in Table 2.

Parameter	Value
d	69.90 [m]
ω_1/ω_0	23.9592 [°/orbit]
Max. Dist.	149.23 [m]
Min. Dist.	1.77 [m]

Table 2: Parameters describing the selected torus around the reference DRO.

3. Guidance and control

The quasi-periodic tori introduced in Section 2.5 provide a natural region of space to virtually maintain a bounded formation. Nevertheless, it was pointed out how the natural motion generates relative reorientation of the formation agents. It is therefore desirable to introduce an active control to manage such motion, and ensure faster reconfigurations or fixed orientation for a certain amount of time.

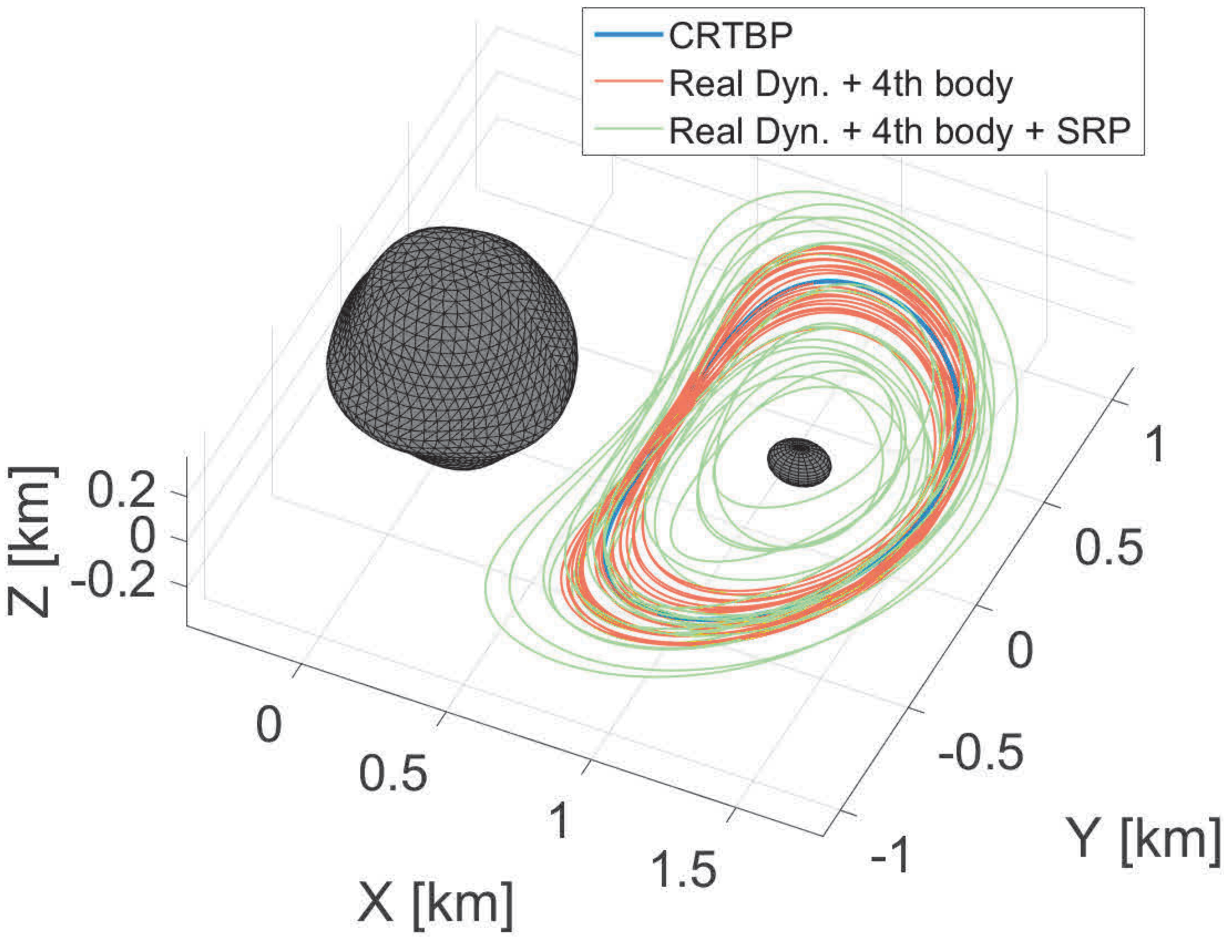

Fig. 2: Evolution of a DRO in increasingly perturbed environments

This can be done through the development of a reference tracking problem, where a spacecraft on the torus targets another point on the same dynamical surface.

A preliminary reference cost map, depicted in Fig. 5, is generated through the optimisation of impulsive manoeuvres transfers. To magnify the differences with respect to the initial longitude and phase on the torus, a full phase shift is considered, i.e. the target point is always at 180° beyond the initial phase. Cost peaks of almost $6\,\mathrm{cm\,s^{-1}}$ are observed in the regions of highest vertical displacement of the torus, and in the region external to the binary system (nearby $\theta_0 = 180°$), while nearly null cost regions are observed across the whole trajectory in the points where the initial and target trajectory branches intersect each other, as depicted in Fig. 6. The results from Fig. 5 are used as a reference for performance comparison with the scheme proposed in the present paper.

3.1. Target state identification

The on-board scheme requires to be computationally efficient, therefore it is desirable to compute the target state without resorting to numerical propagations of the dynamics. Luckily, the closed surface of the torus can be easily parametrised as a function $\mathbb{R}^2 \rightarrow \mathbb{R}^6$ which maps the two longitude and phase angles into a full 6-dimensional state. This approach, already exploited in past research as in Baresi et al. (2021), is here reformulated in relative terms to specialise it to formation flying scenarios. In particular, recalling the methodology proposed by the authors in Capannolo et al. (2023), a 2D cubic spline formulation of the relative torus

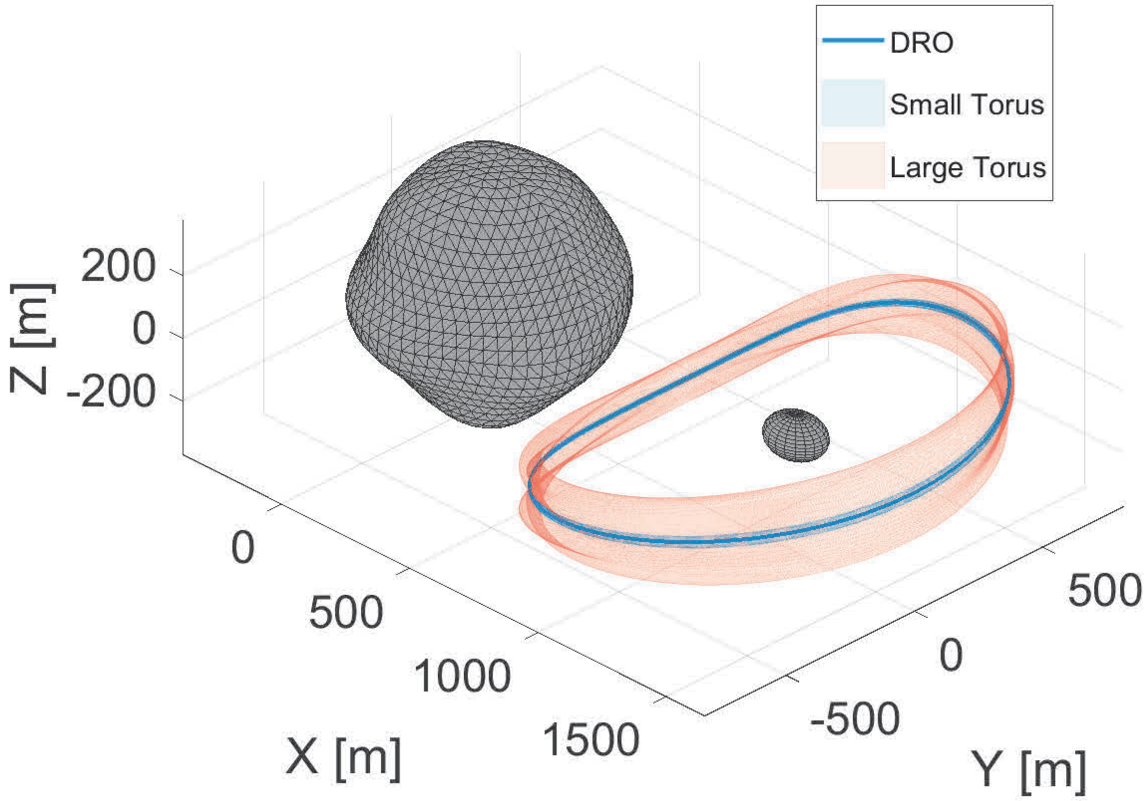

Fig. 3: Smallest and largest DRO tori with respect to the binary system's barycenter

(expressed from now on as $\boldsymbol{s}(\theta_{0f}, \theta_{1f})$) is exploited. The cubic spline is built from a grid of states along the torus, with evenly spaced phase angles. The grid does not follow the natural trajectories of the torus, hence the expression $\boldsymbol{s}(\theta_{0f}, \theta_{1f})$ must rely on time varying angles. In other words, given the target trajectory (defined by the phase angle θ_{1f}), and the initial longitude θ_{0f} (or θ_{0i}), the target angles at each time step are defined as

$$\begin{aligned} \tilde{\theta}_{0f} &= \theta_{0f} + \omega_0 t \\ \tilde{\theta}_{1f} &= \theta_{1f} + \omega_1 t \end{aligned} \tag{11}$$

where ω_0 and ω_1 are the two frequencies of the torus, and t is the time measured from the beginning of the transfer. So, having the torus frequencies (ω_0, ω_1) and the torus spline function $\boldsymbol{s}$, provided the initial longitude and target phase at the beginning of the transfer $(\theta_{0f}, \theta_{1f})$, and the main spacecraft state in the synodic frame of the binary system $(\boldsymbol{x_{ref}})$, the time varying target state reads:

$$\boldsymbol{x_T}(t) = \boldsymbol{x_{ref}}(t) + \boldsymbol{s}(\theta_{0f} + \omega_0 t, \theta_{1f} + \omega_1 t) \tag{12}$$

It is worth noting that the parametrisation of a relative torus provide advantages in terms of maintenance of the formation; the regular and closed shape of quasi-periodic tori in the CRTBP model tends to be easily disrupted in a more complex dynamics. For this reason, direct targeting of torus' states in the synodic frame would result in a relative drift from the main spacecraft. On the contrary, leveraging the relative torus structure ensures that the target state of Eq. 12 is always bounded around the main spacecraft,

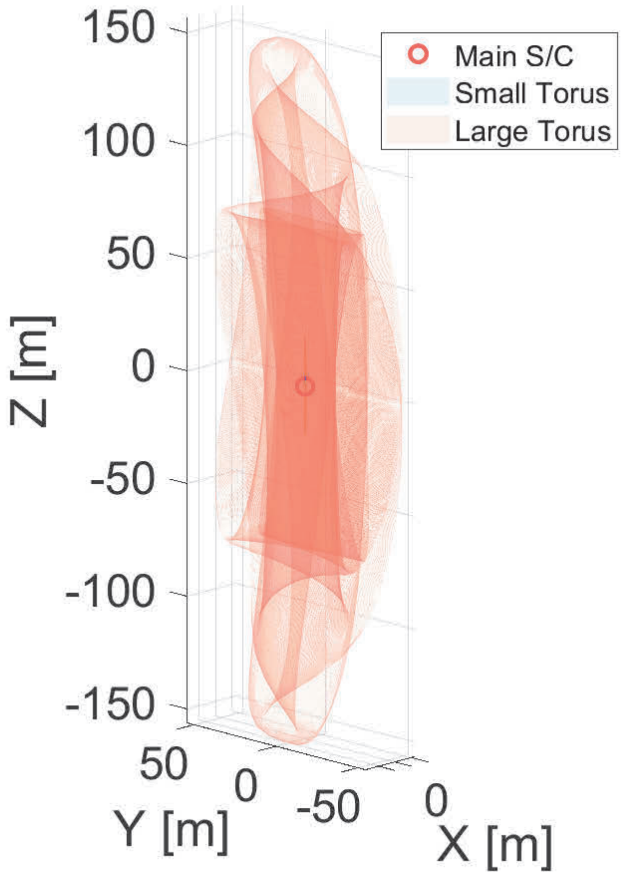

Fig. 4: Smallest and largest DRO tori relatively to a spacecraft on the DRO

despite the discrepancy between the torus' shape and the real dynamics. As a consequence, the full formation motion in the binary system is dictated by the main's state $\mathbf{x_{ref}(t)}$, but such issue goes beyond the scope of this paper and shall be explored in future work.

3.2. Model Predictive Control

Controller formulation. The selected guidance and control scheme follows a receding horizon *Model Predictive Control* (MPC) algorithm, to generate an optimal control action sequence to perform the re-phasing manoeuvres. An in depth presentation of the MPC mathematics can be found in Camacho and Bordons (2002; 2007), while literature where this scheme has been proven extremely powerful for autonomous GNC of either spacecraft or UAV can be found in Gavilan et al. (2015); Vazquez et al. (2015). We preferred this strategy over a shrinking horizon MPC (such as that in Ceresoli et al. (2021)) due to the reduced horizon length, leading to lower demands from a computational standpoint. The receding horizon scheme works with a fixed size window that slides (or *recedes*) at each time instant, shifting its starting and ending point by a single sample time, as represented in Fig. 7. Considering thus the k^{th} time step, the algorithm works in the following fashion.

1. Define a finite-horizon window composed by a fixed number of n_p discrete time-steps. The boundary in this case will be $[t_k,\ t_{k+n_p}]$.
2. Predict the state evolution of the system, exploiting the on-board plant dynamical model and the best estimate of the current state $\hat{\boldsymbol{x}}_k$ as initial condition. Exploiting this initial conditions ensures that the closed-loop behaviour of the controller, which

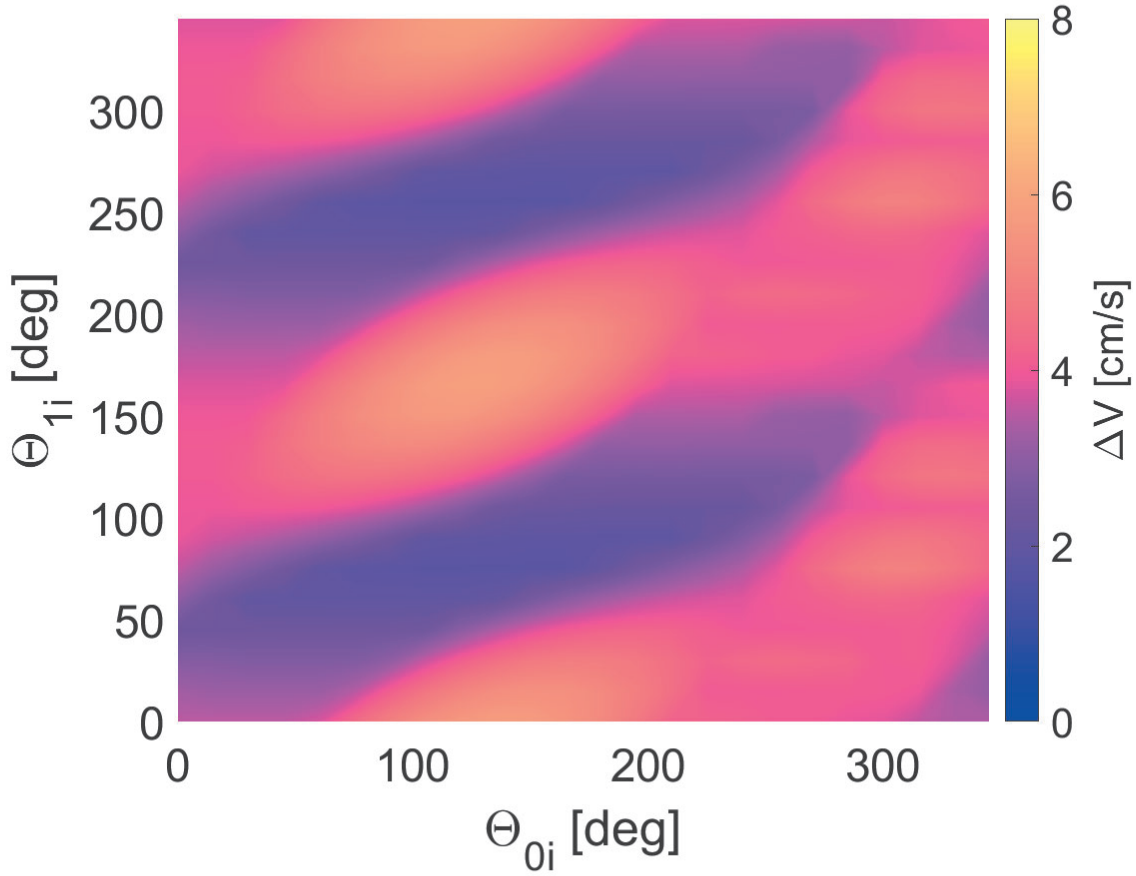

Fig. 5: Cost map for 180° phase shift, as function of the initial point of the spacecraft on the torus

observes the real dynamics and uses it as a feedback, has a more reliable state prediction.

3. Construct and solve an optimal control problem, minimising a certain cost function J whilst exploiting the predicted evolution within the finite horizon. A set of control actions for the whole window duration is obtained, namely $\boldsymbol{u}_k, \boldsymbol{u}_{k+1}, \ldots, \boldsymbol{u}_{k+n_p-1}$.
4. Execute only the first control action. The remaining computed actions are discarded.
5. Define the window by *receding* the finite-horizon by one time-step and come back to point 1 to restart the loop. The new window's boundaries will be $[t_{k+1},\ t_{k+n_p+1}]$.

This procedure is looped for the whole required manoeuvring time, until desired stopping criteria are met, (e.g. threshold relative distance between chaser and target spacecraft in rendezvous scenarios Silvestrini et al. (2020)). A consequence of this is that the overall Time-of-flight is not defined a-priori, but depends on the combined performances of the algorithm and the control authority of the platform.

In order to pass through steps 2 and 3, an on-board discretised state-space model, with a specified sample time T_s, is needed. To do so, Eq. (9) shall be linearised and discretised, leading to the system in Eq. (13), where the state transition matrices from step k to step $k+1$ for the state and for the input are called A_k^{k+1} and B_k^{k+1} respectively.

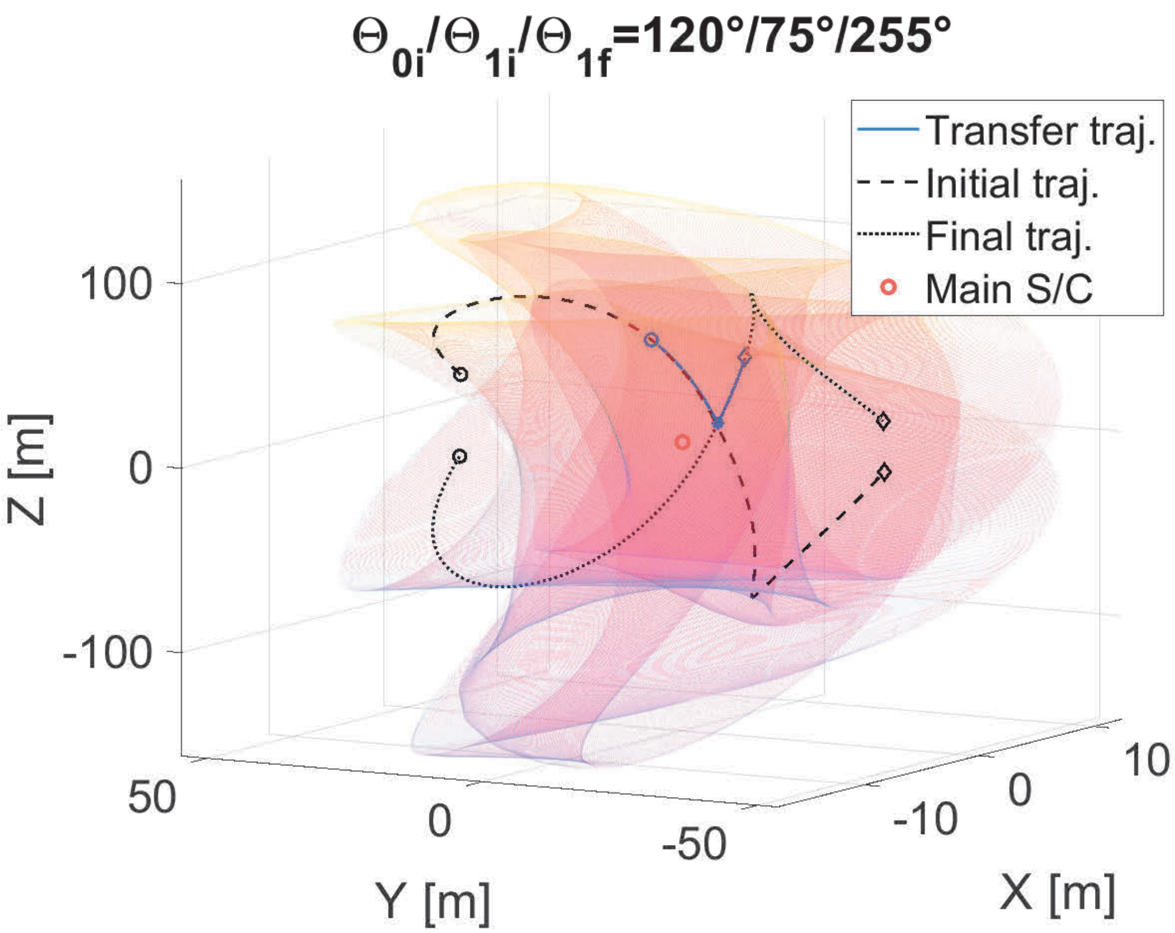

Fig. 6: Example of a transfer with intersecting initial and target trajectories on the torus. Axes not to scale

$$\boldsymbol{x}_{k+1} = A_k^{k+1}(\boldsymbol{x}_k)\boldsymbol{x}_k + B_k^{k+1}(\boldsymbol{x}_k)\boldsymbol{u}_k \tag{13}$$

$$A_k^{k+1} = e^{AT_s} \approx I_{6\times6} + \left.\frac{\partial \boldsymbol{f}(\boldsymbol{x})}{\partial \boldsymbol{x}}\right|_{\boldsymbol{x}_k} T_s \tag{14}$$

$$\begin{aligned} B_k^{k+1} &= \int_{t_k}^{t_{k+1}} e^{A\tau} B \, d\tau \\ &\approx A_k^{k+1} B(\boldsymbol{x}_k) = A_k^{k+1} \begin{bmatrix} 0_{3\times3} \\ I_{3\times3} \end{bmatrix} \end{aligned} \tag{15}$$

Equations (14) and (15) also report the first-order approximation of the state transition matrices, exploiting the jacobian matrix of the dynamics and the trivial definition of the input matrix, considering the control action $\boldsymbol{u}_k$ as an impulsive Δv manoeuvre lasting

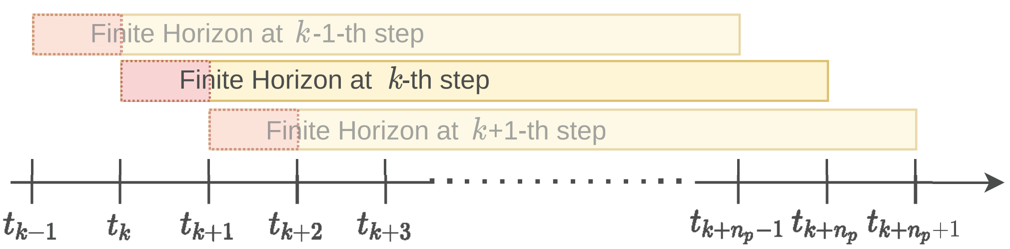

Fig. 7: Receding horizon MPC guidance scheme.

for the complete sample time.

The next step is to construct an optimisation problem in a suitable formulation to reduce the computational burden, done by approaching the problem as in Silvestrini et al. (2020). Due to the deterministic nature of the dynamical system in Eq. (13), from a given initial condition $\boldsymbol{x}_k$ and the complete control history within a prediction window, the complete state evolution up to $\boldsymbol{x}_{k+n_p}$ is determined. It is indeed possible to write chain of equalities to express all the states as function of all the previous control actions and the initial conditions, in order to collect these expressions into a single matrix equation. By stacking all the state vectors vertically, the following arrays are constructed: the stack of n_p state vectors $\mathcal{X}_{k+1} \in \mathbb{R}^{6n_p \times 1}$ and of n_p control vectors $\mathbb{U}_k \in \mathbb{R}^{3n_p \times 1}$ described in Eqs. (16) and (17), and the collection of state transition matrices $\mathbb{A}_k \in \mathbb{R}^{6n_p \times 6}$ and $\mathbb{B}_k \in \mathbb{R}^{6n_p \times 3}$ (these last two expressions are omitted for brevity).

$$\mathcal{X}_{k+1} = \begin{bmatrix} \boldsymbol{x}_{k+1}{}^\top & \boldsymbol{x}_{k+2}{}^\top & \dots & \boldsymbol{x}_{k+n_p}{}^\top \end{bmatrix}^\top \tag{16}$$

$$\mathbb{U}_k = \begin{bmatrix} \boldsymbol{u}_k{}^\top & \boldsymbol{u}_{k+1}{}^\top & \dots & \boldsymbol{u}_{k+n_p-1}{}^\top \end{bmatrix}^\top \tag{17}$$

The complete dynamics within the window is then expressed in a single concise matrix expression, where we define the states stack vector $\mathcal{X}_{k+1}$ as function of the initial state $\boldsymbol{x}_k$ and of the control stack vector $\mathbb{U}_k$, as in Eq. (18).

$$\mathcal{X}_{k+1} = \mathbb{A}_k \boldsymbol{x}_k + \mathbb{B}_k \mathbb{U}_k \tag{18}$$

In order to define a reference tracking problem, transporting this stacked formulation for both the target point and the follower is necessary. Notice that, according to the problem analysed in this paper, the target point is defined for each time step as Eq. (12), and the corresponding control action is null ($\mathbf{u}_T = \mathbf{0}$), being the target a natural trajectory in the dynamics model of the controller (CRTBP). Also, the control actions within the MPC are modelled as impulsive manoeuvre, therefore they can be expressed as

$$\mathbf{\Delta u}_k = \Delta \mathbf{v}_k \delta(t_k) \tag{19}$$

where $\delta(t_k)$ is the *Kronecker's delta*. Defining $\Delta\boldsymbol{x}_k$ as the difference between target trajectory and actual one and the related stack vector as $\mathbb{X}_{k+1}$ (as in Eq. (21)), it is possible to write:

$$\mathbb{X}_{k+1} = \mathbb{A}_k \Delta\boldsymbol{x}_k + \mathbb{B}_k \mathbb{U}_k \tag{20}$$

$$\mathbb{X}_{k+1} = \begin{bmatrix} \Delta\boldsymbol{x}_{k+1}{}^\top & \Delta\boldsymbol{x}_{k+2}{}^\top & \dots & \Delta\boldsymbol{x}_{k+n_p}{}^\top \end{bmatrix}^\top \tag{21}$$

The tracking algorithm is then expressed through a specific cost function, expressed as the summation of quadratic forms of the state error between target trajectory and the current one $\Delta\boldsymbol{x}_{k+i}$ and the control actions $\boldsymbol{u}_{k+i}$ over the prediction window, as in Eq.(22)

$$J(\Delta\boldsymbol{x}_{k,\dots,k+n_p}, \Delta\mathbf{v}_{k,\dots,k+n_p-1}) = \sum_{i=1}^{n_p} \Delta\boldsymbol{x}_{k+i}^\top Q \Delta\boldsymbol{x}_{k+i} + \sum_{i=0}^{n_p-1} \Delta\mathbf{v}_{k+i}^\top R \Delta\mathbf{v}_{k+i} \tag{22}$$

where Q and R are two weighting matrices used to balance the effectiveness and precision of the reference tracking (Q) with the propellant expenditure (R). It is easy then to show that, exploiting the stacked system in Eq. (20), the cost function can be rewritten as

$$J(\mathbb{X}_{k+1}, \mathbb{U}_k) = \frac{1}{2}\Big(\mathbb{X}_{k+1}^\top \hat{Q}\mathbb{X}_{k+1} + \mathbb{U}_k^\top \hat{R}\mathbb{U}_k\Big) \tag{23}$$

where the matrices $\hat{Q}$ and $\hat{R}$ have been defined as block-diagonal matrices with Q and R respectively.

The final step is substituting the states stack in Eq. (23) with the linearised discrete system of Eq. (21), from which the objective function J becomes

$$\begin{aligned} J(\mathbb{U}_k) = \frac{1}{2}\mathbb{U}_k^\top(\mathbb{B}_k^\top \hat{Q}\mathbb{B}_k + \hat{R})\mathbb{U}_k + (\Delta \boldsymbol{x}_k^\top \mathbb{A}_k^\top \hat{Q}\mathbb{B}_k)\mathbb{U}_k + \\ + \frac{1}{2}\Delta \boldsymbol{x}_k^\top \mathbb{A}_k^\top \hat{Q}\mathbb{A}_k \Delta \boldsymbol{x}_k \end{aligned} \tag{24}$$

from which we can easily spot the three addenda with respect to the only unknown of the problem, i.e. the optimisation variable $\mathbb{U}_k$. The first and the second components represent a quadratic and a linear term respectively, while the last one is a constant term, independent from the optimisation variable, thus discardable. The final expression of the quadratic programming problem in Eq. (25) involves the matrix $\mathbb{H} = \mathbb{B}_k^\top \hat{Q}\mathbb{B}_k + \hat{R}$ and the vector $\boldsymbol{l} = (\Delta \boldsymbol{x}_k^\top \mathbb{A}_k^\top \hat{Q}\mathbb{B}_k)^\top$.

$$\min_{\mathbb{U}_k} \quad J(\mathbb{U}_k) = \frac{1}{2}\mathbb{U}_k^\top \mathbb{H}_k \mathbb{U}_k + \boldsymbol{l}^\top \mathbb{U}_k \tag{25}$$

After that, a *maximum thrust* constraints ensures that every $\mathbf{\Delta v}_k$ does not exceed the value manageable by the fixed thrust within a full sample time T_s, namely:

$$||\mathbf{\Delta v}_{k+i}||_2 < \tilde{u}T_s \,, \quad i \in 0 : j \tag{26}$$

Involving the *2-norm* of a vector, the constraint is nonlinear, so it shall be linearised according to a quadratic programming problem. This is done by imposing that the ∞-*norm* of every $\mathbf{\Delta v}_k$ in the prediction window, i.e. every component of the control stack, shall be lower than the maximum impulsive Δv obtainable divided by the square root of three, namely:

$$||\mathbb{U}||_\infty < \frac{\tilde{u}T_s}{\sqrt{3}} \tag{27}$$

Notice that this formulation makes the constraint anisotropic, since any control action aligned with one of the Cartesian directions is required to be less than the actual maximum control that the spacecraft can provide; still, when the control vector is aligned with the trisectrix of the first octant (defined by the three Cartesian axes), the *2-norm* stays below the max value.

Taking into consideration also safety issues, another constraint is here proposed to provide *Collision Avoidance Manoeuvre* (CAM) capabilities. This constraints imposes a minimum distance between the leader and the follower of the formation for the whole transfer arc, which generally is expressed in nonlinear form as follows:

$$||C\mathbf{\Delta x}_{k+i}||_2^2 = \mathbf{\Delta x}_{k+i}^\top C^\top C\mathbf{\Delta x}_{k+i} > R_{KOZ}^2 \,, \quad i \in 0 : j \tag{28}$$

where $C := [I_{3\times3} \quad 0_{3\times3}]^\top$, while R_{KOZ} is the radius of the *Keep Out Zone* (KOZ) sphere. Also in this case, to exploit the constraint in the quadratic programming formulation, a linearisation is performed with a strategy proposed by Morgan et al. (2014), where the KOZ sphere is approximated into a plane tangent to it, and normal to the $\Delta\mathbf{x}_{k+i}$ vector. The constraint can thus be written in a convex form as per Eq. (29), exploiting the known initial value of the prediction window, $\mathbf{\Delta x}_k$.

$$-\mathbf{\Delta x}_k^{\top} C^{\top} C \mathbf{\Delta x}_{k+i} < -R_{KOZ} \, ||C \mathbf{\Delta x}_k||_2 \tag{29}$$

Note that, to express the constraint as an upper boundary inequality, the sign of both sides of the equation has been inverted. To express this constraint at each time instant within the prediction window, Eq. (29) is reformulated as function of the control stack, leading to the following expressions:

$$A_{CAM} \mathbb{U} < \mathbf{b}_{CAM} \tag{30}$$

with

$$\begin{aligned} A_{CAM} &= - I_{n_p \times n_p} \otimes \mathbf{\Delta x}_k^{\top} C^{\top} C \mathbb{B}_k \quad (31) \\ \mathbf{b}_{CAM} &= - R_{KOZ} \, ||C \mathbf{\Delta x}_k||_2 \, \mathbf{1}_{n_p \times 1} + \\ & \quad I_{n_p \times n_p} \otimes \mathbf{\Delta x}_k^{\top} C^{\top} C \mathbb{A}_k \mathbf{\Delta x}_k \quad (32) \end{aligned}$$

where the symbol $\otimes$ indicates the *Kronecker product*.

At this point, the complete problem, with quadratic cost function and linear constraints (both maximum thrust and CAM), reads:

$$\begin{aligned} \min_{\mathbb{U}} \quad & \frac{1}{2} \mathbb{U}^{\top} \mathbb{H}_k \mathbb{U} + \mathbf{l}_k^{\top} \mathbb{U} \\ \text{s.t.} \quad & ||\mathbb{U}||_{\infty} < \frac{\tilde{u} T_s}{\sqrt{3}} \\ & A_{CAM} \mathbb{U} < \mathbf{b}_{CAM} \end{aligned} \tag{33}$$

which is the expression ready to be tackled by any *quadratic programming* solver at each time step over the given finite horizon window. Starting thus from the initial error $\Delta \boldsymbol{x}_k$, the linearised model to evaluate the state transition matrix of Eq. (14), solving the optimisation problem will provide the optimal control stack vector $\hat{\mathbb{U}}_k$, which will be exploited only for its very first component, i. e. $\hat{\Delta \mathbf{v}}_k$.

Weight matrices. The problem expressed by Eq. (33) presents the weighting matrices Q and R as tuning parameters. The simplest strategy would be to define a fixed value for both, obtained either by trial and error or by a specific optimisation problem with the aim of finding the best value trading-off convergence to the target trajectory and propellant usage. However such approach may lead to very long processes and less versatile algorithms, since the tuning of these parameters would vary widely changing the requested formation reconfiguration manoeuvre. Consequently we used the same approach presented in Capannolo and Lavagna (2022), where an adaptation law is defined in order to automatically adjust the balance among control responsiveness and cost reduction on-board.

This *Adaptive Weights* strategy requires a single initial tuning of some terms, but provides efficient transfers of the spacecraft anywhere along the quasi-periodic torus. In this approach the R matrix is kept equal to the identity matrix, while Q is defined by a diagonal matrix with a position term q_r equal for the first three elements of the diagonal and a velocity term q_v for the remaining ones. In particular, the position terms q_r of the weight matrix Q are scaled through a coefficient directly related to the spacecraft-target relative state, and to the available time to complete the transfer within the maximum ToF:

$$q_r = \gamma(\Delta r, \Delta \dot{r}, t) q_{MAX} \tag{34}$$

with q_{MAX} being a user-defined upper limit for the weight, and γ being the adaptation coefficient, explicitly defined as:

$$\gamma = \alpha^{\beta} \tag{35}$$

$$\alpha = \left(\frac{\Delta r_T}{\Delta r}\right) \tag{36}$$

$$\beta = 1 + \frac{\Delta\dot{r}}{\Delta r}(ToF - t) \tag{37}$$

Here, Δr and $\Delta\dot{r}$ respectively represent the radial distance and speed from spacecraft to target point, Δr_T is the distance threshold for a successful transfer, and t is the current time. In such a way, the control action results smaller at large distance from target and at early stages of the transfers, avoiding large initial control actions. On the other hand, it pushes the weight to its maximum value when approaching the target and/or when the time left is short. Moreover, including information about the local radial relative velocity avoids excessively slow or high approaching speeds. In addition, a saturation effect on the reduction term $\Delta\beta$ between consecutive sample points is given, aimed at avoiding large control cost increments due to local small approach speed of the target:

$$\beta = \max\left(\left[1 + \frac{\Delta\dot{r}}{\Delta r}(ToF - t) \quad , \quad \beta_0 - \Delta\beta\right]\right) \tag{38}$$

where β_0 denotes the β exponent from the previous step. There is instead no adaptation included for the velocity terms of the weight matrix q_v, which are tuned once and remain fixed during the transfer. This choice was made to prevent potential instabilities in the transfer that may arise when the value of these weights approaches zero, leading to undesired overshoots. The work in Capannolo and Lavagna (2022) presents the adaptation law more in details and compares it with a fixed weight approach, applied to a similar guidance and control scheme.

For the case under study, Table 3 reports the tuned parameters for the adaptation law.

Parameter	Value
q_{MAX}	$10^{2.5}$ [-]
q_v	10^{-1} [-]
$\beta_0\|_{init}$	2 [-]
$\Delta\beta$	2 [units/h]

Table 3: Parameters for the MPC control strategy with adaptive weights.

Performance analysis. To address the performance of the on-board MPC, the transfers are first executed without collision avoidance, and the costs are compared to the reference impulsive transfers of Fig. 5. The new costs are depicted in Fig. 8. Overall, it is possible to notice a global increment of the costs for the regions already showing the highest costs in the impulsive transfers case. This is justified by the fact that the on-board controller is not able to plan the best times to manoeuvre, and always delivers a control action at each time step of the clock set for the controller itself. The new costs reach the value of $8\,\mathrm{cm\,s^{-1}}$, approximately $25 - 30\%$ more than the impulsive transfer maximum cost. Furthermore, one can notice that the new map displays a greater cost increment in the regions of the DRO between the attractors ($\theta_{0i} > 270°$); this is due to the fact that the on-board scheme always relies on the maximum (user-defined) ToF available for the transfer, while in such region, the impulsive transfer optimiser returns lower costs with a reduced ToF. Nevertheless, it is worth noting that the cost increment is not particularly critical and can be easily managed even

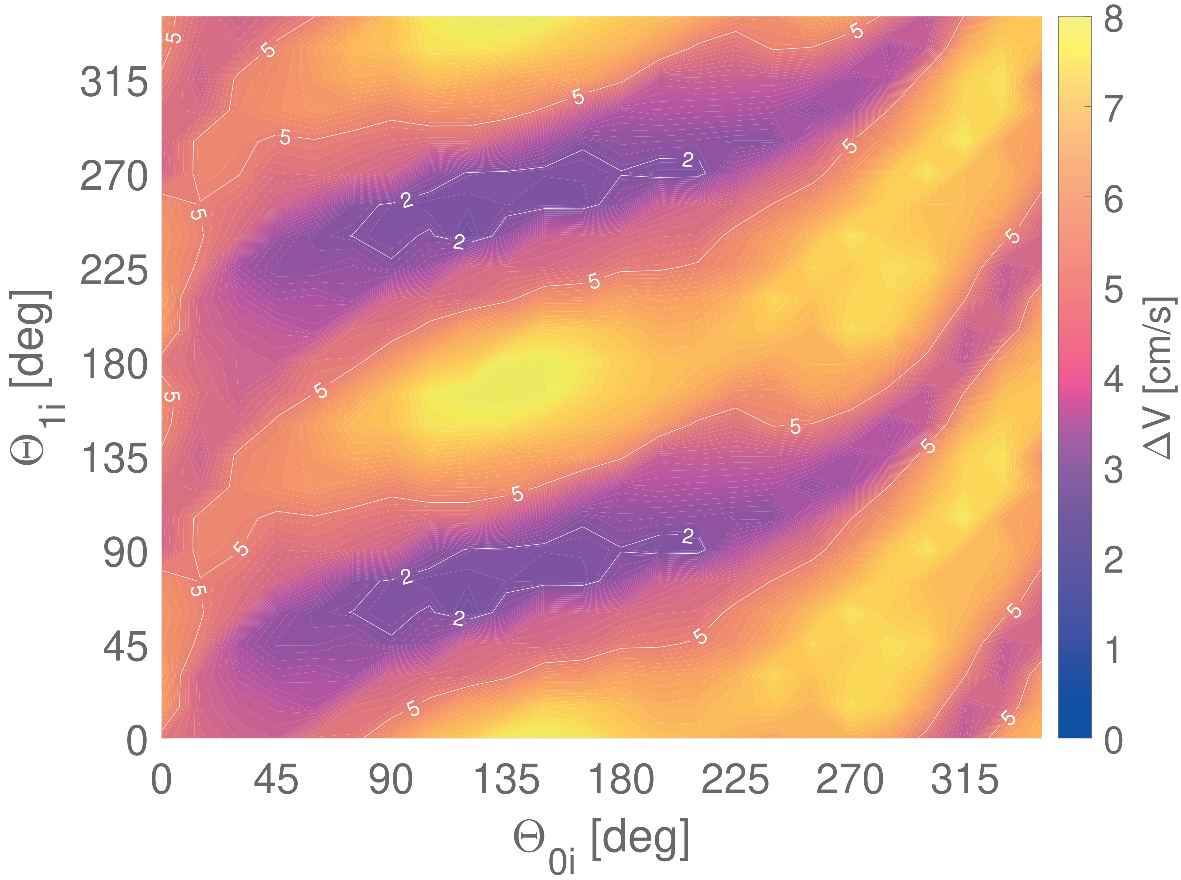

Fig. 8: Cost map for the on-board MPC with adaptation law

by very small platforms. A peculiar behaviour is instead observed for low-cost regions, where intersection of trajectories occurs, as depicted in Fig. 6. Here thanks to such intersection, the on-board controller is able to approximately get the same reduced costs as the impulsive case. It is worth mentioning that the limited increments in costs are mostly possible thanks to the adaptation law of Eq. (34), which mitigates large control actions for the long-distance transfers, while a standard setup of weights would further increase the difference from the impulsive cost map, as observed in Capannolo (2022).

A second step of the analysis is carried out to address the capability of the on-board controller (and of the adaptation law) to withstand deviations due to collision avoidance manoeuvres. In particular, a minimum distance of 20 m is set between the two spacecraft, which covers most of the torus regions. It has been observed that, with very few exceptions, the increment of costs due to CAMs is always below $+5\,\mathrm{cm\,s^{-1}}$, and in very few regions above $+2\,\mathrm{cm\,s^{-1}}$, as depicted in Fig. 9. Regardless, all transfer are executed and completed with success despite the deviations, thanks to the adaptation law. The longer path causes the spacecraft to be at relatively large distance for a longer time; this pushes the weights to a higher value, ensuring the completion of the last branch of the transfer in the shorter time available. Overall, the transfer times are almost unaltered with respect to their counterpart without CAM, and the rendezvous with the target point occurs in nearly the same spot, as depicted in Fig. 10.

A final validation of the scheme is carried out in the high-fidelity, ephemeris-based dynamics, considering the true trajectories of the attractors, their uneven shape, and the gravitational and SRP effects of the Sun. In general, the MPC scheme was found to withstand the errors between the ”true”, high-fidelity dynamics, and the on-board CRTBP dynamics that the controller is based on.

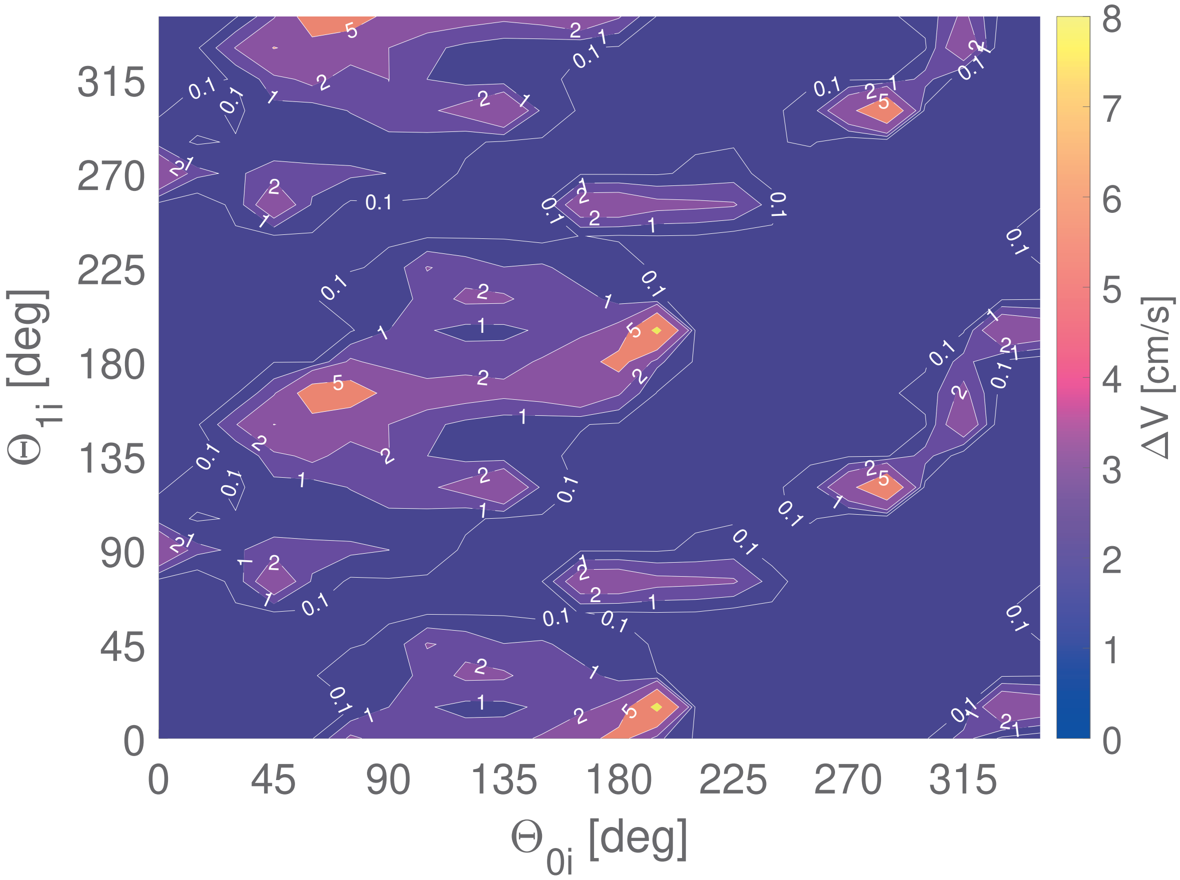

Fig. 9: Cost increment for the on-board MPC when collision avoidance manoeuvres are added.

Figure 11 depicts the new costs for the transfer in the high-fidelity dynamics. It can be observed how the most affected regions are indeed those where cost peaks were present, i.e. the transfers with the maximum vertical displacement. In fact, the longer path is intrinsically more susceptible to perturbations in the dynamics, and a higher effort is demanded to the controller to reach the target point. As a consequence, most of the high cost region demands more than $8\,\mathrm{cm\,s^{-1}}$, with the worst region above $10\,\mathrm{cm\,s^{-1}}$, while low cost regions are nearly unaffected by the new dynamics. It is important to mention that very few spots where the transfer failed have been identified; nevertheless, all of them are located in the very high cost regions of the map.

As a final remark, the scheme presented in this section has been tested assuming a perfect knowledge of the spacecraft state. The next section will be devoted to the performance degradation analysis in presence of navigation uncertainties.

4. Navigation requirements

This last section presents a simple approach to assess the guidance and control scheme robustness against state estimation uncertainties. In Fig. 12 a possible complete closed-loop GNC scheme is shown. The inclusion of a navigation filter in the loop, which is fed by the various measurements $\mathbf{y}_k$ provided by on-board sensors, outputs the initial conditions $\hat{\boldsymbol{x}}_k$ of the spacecraft in the prediction window to the MPC scheme. Note that these initial conditions are not the real ones, as the navigation will introduce deviations from the real trajectory.

To emulate such behaviour, the simulations of the transfers presented in the previous section are performed a second time, con-

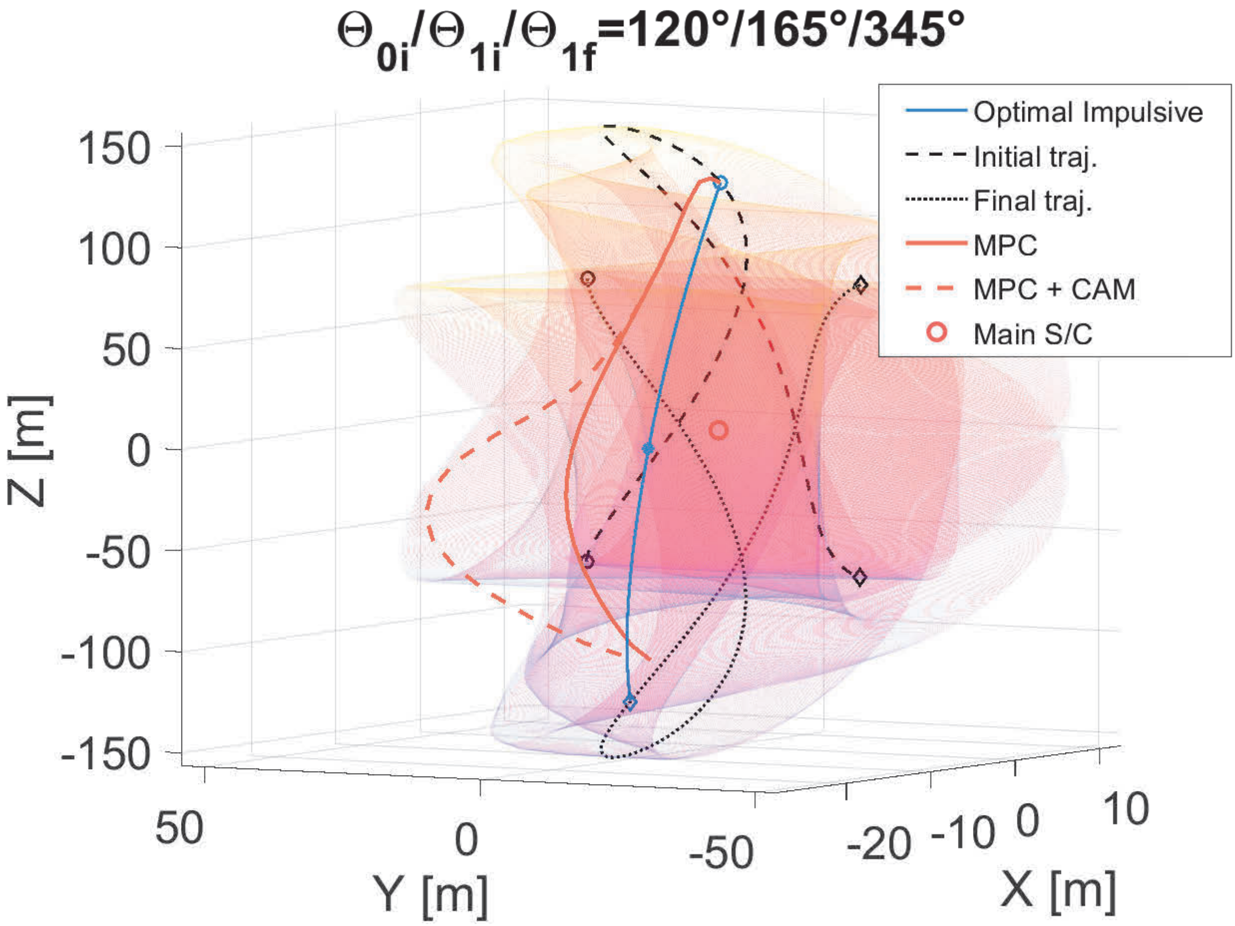

Fig. 10: Transfer comparison between impulsive manoeuvres, MPC, and MPC with CAM

sidering noisy states as initial conditions. These conditions have been obtained by generating Gaussian random noise components for each of the six elements of the state, with a null mean and an arbitrary standard deviation level (grouped into a value for the position σ_r and a value for the velocity σ_v). By letting these values vary by orders of magnitude, the final position error Δr_f and total transfer cost Δv_{tot} have been mapped. Table 4 reports the results for a specific transfer ($\theta_{0i} = 45°$, $\theta_{1i} = 135°$), including the case of a perfect state knowledge as reference for comparison.

Considering the 2 m error threshold defined in the guidance scheme, the results highlight how complex and demanding the relative dynamics in this small binary asteroid system is. Indeed, the target distance below the threshold of 2 m is reached only with $\sigma_r = 1$ m and $\sigma_v = 1\,\mathrm{mm\,s^{-1}}$ for both scenarios, with and without the collision avoidance constraint. This result was expected regarding the position estimation error, due to the very strict requirement in terms of the final trajectory error, but these analyses provided a boundary value also for the velocity, leading to very demanding requirements for a navigation system. From Table 4, other useful insights on the proposed *Guidance and Control* (G&C) scheme can be described. First, by looking at rows B and C, it can be noticed that a higher accuracy in the velocity components (case B) is more beneficial than reducing the position error (case C). Indeed, in case C the transfer cost is even higher than case B. This shows how having a better position reconstruction pushes the controller to activate thrusters for longer periods, but without achieving good results due to the poor velocity knowledge. The simulations that include CAM show the same trend between cases B and C in terms of Δr_f, but differ in terms of Δv_{tot}. This can be explained by the very high sensitivity that the CAM algorithm presents toward the position knowledge, which is directly involved

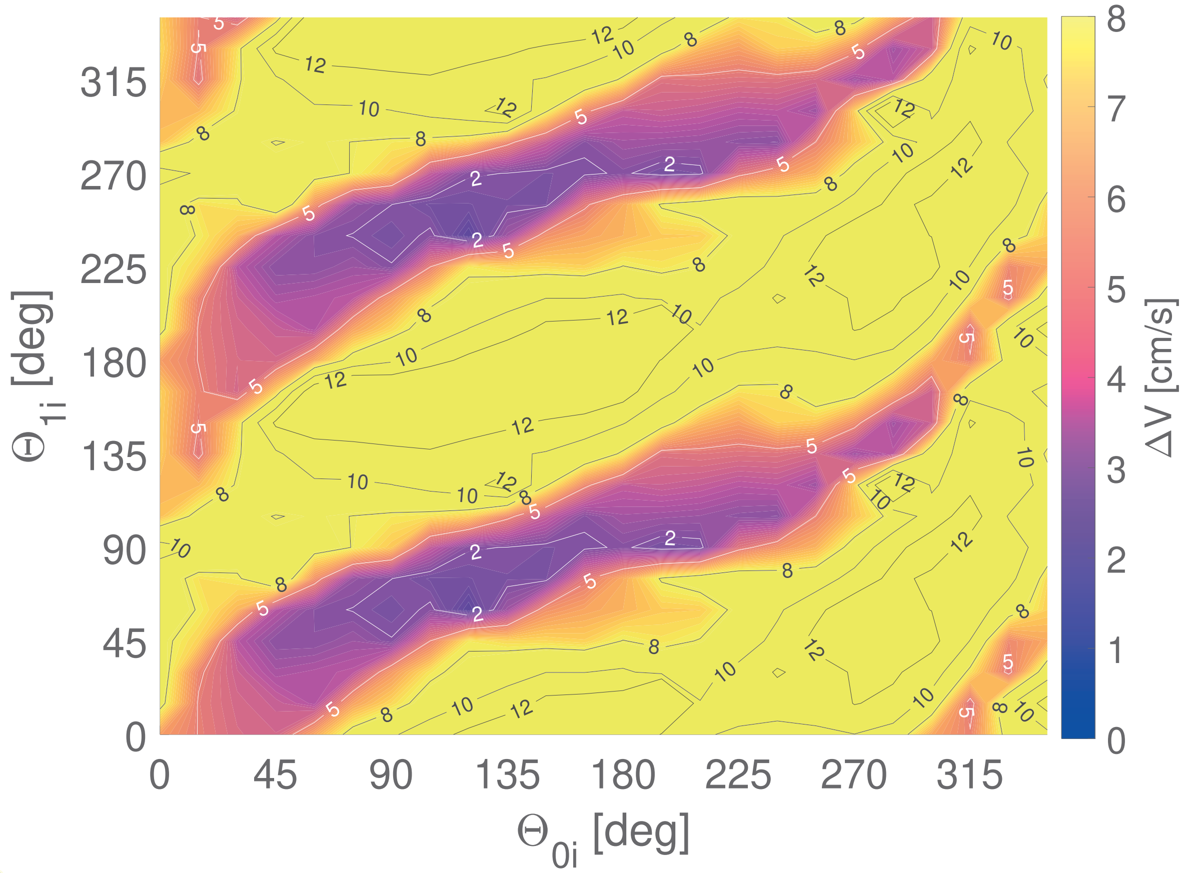

Fig. 11: Transfer costs map in the high-fidelity dynamics

in the evaluation of the constraint.

5. Conclusions

This paper presented a comprehensive way to generate relative trajectories in a complex and harsh environment such as the one of of a binary asteroid system, exploiting the parametrisation of quasi-periodic invariant tori. This framework is useful to define a simple and yet effective approach for retrieving relative target trajectory, and exploiting such trajectories for a reference tracking guidance and control scheme. A receding horizon Model Predictive Control was exploited to solve the optimal control problem. By discretising and linearising the relative dynamics, the fully nonlinear problem was reduced to a computationally lighter quadratic programming problem.To preserve the quadratic formulation, maximum thrust and collision avoidance constraints were also expressed in a linear and convex fashion, that was proven to be effective. An adaptation law for the MPC tuning parameters, embedded to the scheme, showed promising results. A first test, comparing the on-board, thrust-constrained MPC to the impulsive, optimised transfers showed an overall maximum cost increment of less than 30% of the former. Such values are considered more than satisfactory, considering that the MPC works on a local finite horizon, which does not foresee the whole evolution of the trajectory. Secondly, it was observed that even in presence of collision avoidance manoeuvres, cost increments were mostly below $2\,\mathrm{cm\,s^{-1}}$, corresponding to an additional 20% with respect to the value without CAM. Finally, tests in high-fidelity environment proved the good robustness of the controller against unmodelled dynamics, always ensuring the completion of the transfers. The

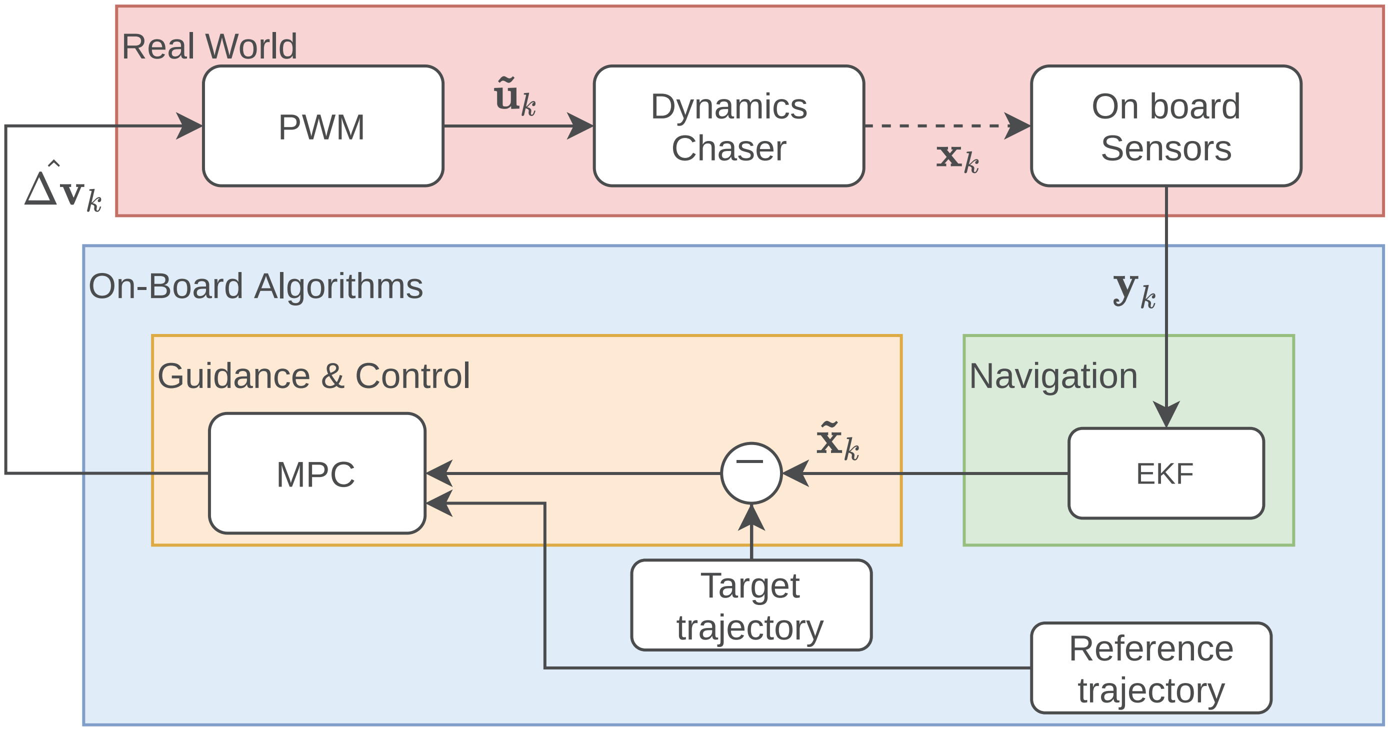

Fig. 12: Closed-loop GNC scheme.

Table 4: Resulting trajectory position error and total transfer cost for different levels of state estimation errors without or with the CAM constraint.

ID	σ_r [km]	σ_v [m/s]	Δr_f [km]	Δv_{tot} [m/s]	Δr_f [km] (with CAM)	Δv_{tot} [m/s] (with CAM)
REF	0	0	0.0003	0.054	0.0009	0.069
A	0.1	0.1	0.4434	0.992	0.3381	1.309
B	0.1	0.01	0.0584	0.399	0.1484	1.605
C	0.01	0.1	0.4783	1.363	0.1938	1.224
D	0.01	0.01	0.0343	0.171	0.0256	0.166
E	0.001	0.01	0.0070	0.201	0.0080	0.216
F	0.001	0.001	0.0009	0.070	0.0012	0.089

corresponding costs oscillated from almost no change up to ∼ 90%. It is worth noting that high percentage increments are obtained for the most expensive transfers, which should be avoided a priori in the context of a real mission. In addition, a sensitivity analysis has been carried out after closing the GNC loop with state estimation, with the aim of providing requirements to the navigation block. The simulations highlighted the complexity of the analysed scenario, where the uncertainty on the spacecraft state shall achieve very accurate values, down to 1 m for position and $1\,\mathrm{mm\,s^{-1}}$ for velocity.

References

Brian T. Barden. Formation flying in the vicinity of libration point orbits. In *Proceedings of the AAS/AIAA Space Flight Mechanics Meeting, Monterey, 1998*, pages 969–988, 1998.

Nicola Baresi, Zubin P Olikara, and Daniel J. Scheeres. Fully numerical methods for continuing families of quasi-periodic invariant tori in astrodynamics. *The Journal of the astronautical sciences*, 65(2):157–182, 2018.

Nicola Baresi, Diogene A Dei Tos, Hitoshi Ikeda, and Yasuhiro Kawakatsu. Trajectory design and maintenance of the martian moons exploration mission around phobos. *Journal of guidance, control, and dynamics*, 44(5):996–1007, 2021.

Solomon L'vovich Belousov. *Tables of Normalized Associated Legendre Polynomials: Mathematical Tables Series*. Elsevier, 2014.

Eduardo F. Camacho and Carlos Bordons. *Model predictive control*. 2002. ISBN 9783540762416.

Eduardo F. Camacho and Carlos Bordons. Introduction to model predictive control. In *Model Predictive Control*, pages 1–11. Springer, 2007.

Andrea Capannolo. *Dynamics, guidance and control of reconfigurable spacecraft formations in multibody environments*. PhD thesis, Politecnico di Milano, 2022.

Andrea Capannolo and Michèle Lavagna. Minimum cost relative dynamics in cislunar environment. In *71st International Astronautical Congress (IAC 2020)*, pages 1–11, 2020.

Andrea Capannolo and Michèle Lavagna. Adaptive state-dependent riccati equation control for formation reconfiguration in cislunar space. *Journal of Guidance, Control, and Dynamics*, pages 1–8, 2022.

Andrea Capannolo, Fabio Ferrari, and Michèle Lavagna. Families of bounded orbits near binary asteroid 65803 didymos. *Journal of Guidance, Control, and Dynamics*, 42(1):189–198, 2019.

Andrea Capannolo, Andrea Pasquale, Margherita Piccinin, Stefano Silvestrini, Giovanni Zanotti, and Michèle Lavagna. Mission analysis and trajectory design for nanosat scientific exploration around binary systems leveraging the dynamical environment. In *2020 AAS/AIAA Astrodynamics Specialist Conference*, pages 1–18, 2020.

Andrea Capannolo, Giovanni Zanotti, Michèle Lavagna, Elena Mazzotta Epifani, Elisabetta Dotto, Vincenzo Della Corte, Igor Gai, Marco Zannoni, Marilena Amoroso, and Simone Pirrotta. Challenges in licia cubesat trajectory design to support dart mission science. *Acta Astronautica*, 182:208–218, 2021. ISSN 0094-5765. `https://doi.org/10.1016/j.actaastro.2020.09.023`. URL `https://www.sciencedirect.com/science/article/pii/S0094576520305622`.

Andrea Capannolo, Giovanni Zanotti, Michèle Lavagna, and Giuseppe Cataldo. Model predictive control for formation reconfiguration exploiting quasi-periodic tori in the cislunar environment. *Nonlinear Dynamics*, pages 1–19, 2023. `https://doi.org/10.1007/s11071-022-08214-8`.

Michele Ceresoli, Giovanni Zanotti, and Michèle Lavagna. Bearing-only navigation for proximity operations on cis-lunar non-keplerian orbits. In *72nd International Astronautical Congress (IAC 2021)*, pages 1–10, 2021.

Loic P. R. Chappaz. *High-fidelity gravity modeling applied to spacecraft trajectories and lunar interior analysis*. PhD thesis, Purdue University, 2015.

Andy F. Cheng, Justin Atchison, Brian Kantsiper, Andrew S. Rivkin, Angela Stickle, Cheryl Reed, Andres Galvez, Ian Carnelli, Patrick Michel, and Stephen Ulamec. Asteroid impact and deflection assessment mission. *Acta Astronautica*, 115:262–269, 2015.

Elisabetta Dotto, Vincenzo Della Corte, Marilena Amoroso, Ivano Bertini, John R. Brucato, Andrea Capannolo, Biagio Cotugno, Gabriele Cremonese, Valerio Di Tana, Igor Gai, et al. Liciacube-the light italian cubesat for imaging of asteroids in support of the nasa dart mission towards asteroid (65803) didymos. *Planetary and Space Science*, 199:105185, 2021.

William M. Folkner, James G. Williams, Dale H. Boggs, Ryan S. Park, and Petr Kuchynka. The planetary and lunar ephemerides de430 and de431. *Interplanetary Network Progress Report*, 196(1):42–196, 2014.

Francisco Gavilan, Rafael Vazquez, and Eduardo F. Camacho. An iterative model predictive control algorithm for uav guidance. *IEEE transactions on aerospace and electronic systems*, 51(3):2406–2419, 2015.

Ernest William Hobson. *The theory of spherical and ellipsoidal harmonics*. Cambridge University Press, 1931.

William Duncan MacMillan. *The theory of the potential*, chapter 35–36, pages 56–60. Dover, 1958. `10.1021/ed007p2530`.

Patrick Michel, Michael Kueppers, Ian Carnelli, Adriano Campo Bagatin, Benoit Carry, Sebastien Charnoz, Alan Fitzsimmons, Simon Green, Carsten Güttler, Alain Herique, et al. The esa hera mission to the binary asteroid didymos: planetary defense and bonus science. In *International Astronautical Congress (IAC 2020)*. International Astronautical Federation, IAF, 2020.

Daniel Morgan, Soon Jo Chung, and Fred Y. Hadaegh. Model predictive control of swarms of spacecraft using sequential convex programming. *Journal of Guidance, Control, and Dynamics*, 37(6):1725–1740, 2014. ISSN 15333884. `10.2514/1.G000218`.

Martin T. Ozimek and Justin A. Atchison. Nasa double asteroid redirection test (dart) low-thrust trajectory concept. In *27th AAS/AIAA Space Flight Mechanics Meeting, San Antonio, USA*, volume 221, 2017.

Margherita Piccinin, Giovanni Zanotti, Stefano Silvestrini, Andrea Capannolo, Andrea Pasquale, and Michèle Lavagna. Cubesat exploration missions to binary asteroids: on board autonomy and intelligent imaging towards science return enhancement. In *2020 AAS/AIAA Astrodynamics Specialist Conference*, pages 1–14, 2020.

Petr Pravec, Petr Scheirich, Peter Kušnirák, Lenka Šarounová, Stefano Mottola, Gerhard J. Hahn, Peter G. Brown, Gilbert A. Esquerdo, Nicholas Kaiser, Zbigniew Krzeminski, et al. Photometric survey of binary near-earth asteroids. *Icarus*, 181(1):63–93, 2006.

Petr Scheirich and Petr Pravec. Modeling of lightcurves of binary asteroids. *Icarus*, 200(2):531–547, 2009.

Stefano Silvestrini, Jacopo Prinetto, Giovanni Zanotti, and Michèle Lavagna. Design of robust passively safe relative trajectories for uncooperative debris imaging in preparation to removal. In *2020 AAS/AIAA Astrodynamics Specialist Conference*, pages 1–18, Virtual Lake Tahoe, United States, 2020.

Stefano Silvestrini, Margherita Piccinin, Andrea Capannolo, Michèle Lavagna, and Jesus G. Fernandez. Centralized autonomous relative navigation of multiple cubesats around didymos system. *The Journal of the Astronautical Sciences*, 68(3):750–784, 2021.

Victor Szebehely. *Theory of Orbits: The Restricted Problem of Three Bodies*. Academic Press, New York and London, 1967.

Rafael Vazquez, Francisco Gavilan, and Eduardo F. Camacho. Model predictive control for spacecraft rendezvous in elliptical orbits with on/off thrusters. *IFAC-PapersOnLine*, 48(9):251–256, 2015.